Supplementary Information for

Correlated Li-ion migration in the superionic conductor $Li_{10}GeP_2S_{12}$

Takeshi Yajima[1,*], Yoyo Hinuma[2,#], Satoshi Hori[3], Rui Iwasaki[1], Ryoji Kanno[4], Takeshi Ohhara[5], Akiko Nakao[6], Koji Munakata[6], and Zenji Hiroi[1]

[1]Institute for Solid State Physics, University of Tokyo, Kashiwa, Chiba 277-8581, Japan.

[2] Center for Frontier Science, Chiba University, 1-33 Yayoi-cho, Inage, Chiba 263-8522, Japan.

[3]Institute of Innovative Research (IIR), All-Solid-State Battery Unit, Tokyo Institute of Technology, 4259 Nagatsuta, Midori, Yokohama 226-8502, Japan.

[4]Research Center for All-Solid-State Battery, Institute of Innovative Research (IIR), Tokyo Institute of Technology, 4259 Nagatsuta, Midori, Yokohama 226-8502, Japan

[5]J-PARC Center, Japan Atomic Energy Agency, Tokai, Ibaraki 319-1195, Japan.

[6]Center for Neutron Science and Technology, Comprehensive Research Organization for Science and Society (CROSS), Tokai 319-1106, Japan.

Correspondence to:
*(T.Y.) yajima@issp.u-tokyo.ac.jp

#Present Address

Department of Energy and Environment, National Institute of Advanced Industrial Science and Technology (AIST) 1-8-31, Midorigaoka, Ikeda, Osaka 563-8577, Japan

Structural analysis at RT

Structural analysis was performed using X-ray diffraction (XRD) data collected at RT at around 300 K to determine the overall crystal structure, including the Ge/P ratio, which determines the amount of Li that is required to retain charge neutrality. The obtained chemical formula of the crystal was $Li_{10.34}Ge_{1.34}P_{1.66}S_{12}$, which is consistent with the average chemical composition obtained from many crystals using inductively coupled plasma atomic emission spectroscopy (ICP-AES; Li : Ge : P = 11.2 : 1.28 : 1.72). Neutron diffraction (ND) data was then refined to provide more reliable information about Li atoms, including their coordinates, occupancies, and anisotropic displacement parameters (ADPs). The combined refinements were finally converged with reasonably small R factors: $R_1 = 2.26\%$ and $wR_2 = 2.90\%$ for XRD and $R_1 = 8.17\%$ and $wR_2 = 6.58\%$ for ND. The refined structure was essentially the same as those reported in previous studies[19,21,22]. The Li2 and Li4 sites were at the 4*d* and 4*c* Wyckoff positions, respectively, whereas each of Li1 and Li3 sites showed a

characteristic splitting into two 16*h* sites. This site splitting of Li3 was not observed in previous studies, and was recently shown in the single-crystal XRD analysis[33]. In the present analysis, refinement without the splitting of the Li3 site converged to worse *R*-values (R_1 = 8.41% and wR_2 = 6.74%) than the split model. Thus, the "Li3 split model" is the most reasonable structural model at RT. The refined structural parameters are given in Tables S1a and S1b.

Structural analysis at 10 K

First, the ND data was refined at 10 K assuming a structural model identical to the one at RT, which converged to reasonably small *R* factors (R_1 = 8.58% and wR_2 = 6.33%). Next, we performed maximum-entropy method (MEM) analyses for both the RT and 10 K ND data. This is especially advantageous for structural analyses of ionic conductors because the reconstructed electron/scattering-length density obtained via MEM is not associated with individual atomic sites with thermal ellipsoids, but to a probable spatial distribution of atomic density. The scattering-length density distribution at 10 K (Fig. 1b) revealed further site splitting of the Li3 site, to one 8*f* site (Li3b) and two nearby positions with smaller densities corresponding to Li3a at the 16*h* site present at RT. Hence, we carried out another structural analysis on the ND data at 10 K assuming a triple-split model with Li atoms at the 8*f* (Li3b) and 16*h* (Li3a) sites. Note that the Li3b site corresponds to the split Li3 site at RT in the previous double-split model. The triple-split model gave a significant improvement in the refinement, with noticeably smaller *R* values (R_1 = 8.38% and wR_2 = 6.15%) than the double-split model; the chemical composition was thus deduced as $Li_{10.49}Ge_{1.34}P_{1.66}S_{12}$. The refined structural parameters are shown in Table S1c.

Possible diffusion pathways deduced from the refined structure

Based on the refined structure at 10 K, possible diffusion pathways for the Li ions were considered. Figure S1 depicts the coordination environments of the Li1–Li4 ions in the framework made of the S ions, and Table S2 summarizes the relevant interatomic distances. Li2 and Li4 were located in the S_6 octahedra, whereas Li1 and Li3 were in the S_4 tetrahedra. The $(Li2)S_6$ octahedron shared edges with four $(Li1)S_4$ and four $(Li3b)S_4$ tetrahedra, and the $(Li4)S_6$ octahedron shared edges with eight $(Li1)S_4$ tetrahedra. The $(Li1)S_4$ and $(Li3b)S_4$ tetrahedra shared edges to form a 1-D chain along the *c* axis. The Li3a ion at the 16*h* site was located near the face of the $(Li3b)S_4$ tetrahedra, resulting in the trigonal bipyramidal coordination depicted by the blue lines in Fig. S1.

The thermal ellipsoids of Li1, Li3a, and Li3b were elongated along the 1-D channel, whereas those of Li2 and Li4 were elongated perpendicular to the 1-D channel, as shown in Fig. 1a. The *g* factors of Li2 and Li4 were 0.857(10) and 0.781(12), respectively, meaning that more than 10% of sites were vacant. These facts indicate the possibility of 2-D diffusion pathways connecting the 1-D channel via Li2 and Li4. Since the ADP of Li4 was twice as large as that of Li2, the Li1−Li4−Li1 path may be major compared with the Li3a−Li2−Li3a path, although the inter-site distance of Li1−Li4 along the [110] direction [3.072(8) Å] was longer than that of Li2−Li3a along the [110] direction [2.650(19) Å]. In fact, our one-particle potential (OPP) and nudged elastic band (NEB) calculations indicated a low barrier for the Li1−Li4−Li1 path, as is mentioned later.

One-particle potential (OPP) calculations

To evaluate the single-ion migration barriers in the 1-D and 2-D pathways, effective OPPs were calculated from the joint probability density functions of Li in the refined structure using the ND data at RT. In this approach, every atom is treated as an individual Einstein oscillator, subject to Boltzmann statistics in the classical limit, meaning that the calculations are valid only at sufficiently high temperatures. For example, for oxygen ionic conductors, the evaluation is normally performed at several hundred degrees Celsius. However, as LGPS shows large ADPs even at RT, this may be a sufficiently high temperature for Li in LGPS. In fact, a previous study revealed that any atomic motion in LGPS can be expressed by the Boltzmann statistical approach[22].

The OPP maps for the pathways along the [001] and [110] directions at RT are shown in Fig. 2a. The split Li1 or Li3 positions are almost connected to each other with negligible energy barriers, as expected from the short distances, although there is a small barrier for Li1–Li3a along the [001] direction. The extremely small barrier for Li3a−Li3a indicates that Li ions can easily migrate over the split Li3 sites, which tend to further split into Li3a–Li3b–Li3a at low temperatures. In contrast, the two pathways (along the [110] direction) have relatively large barriers: 0.35 eV and 0.55 eV for Li1−Li4−Li1 and Li3a−Li2−Li3a, respectively. This is because a migration via an octahedral unit such as [Li2]S_6 and [Li4]S_6 is disadvantageous compared with that via a tetrahedral unit such as [Li1]S_4 and [Li3]S_4[11]. The reason for the larger barrier for the Li3a−Li2−Li3a path is that the volumes of the S octahedra are smaller by about 13% for Li2 compared with those involving Li4, suggesting that Li2 is more strongly bound and less susceptible to migration than Li4.

Nudged elastic band (NEB) calculations

NEB calculations were performed to investigate the conduction mechanism in LGPS. First, we calculated the formation energy of vacancies at different Li sites, and then investigated the effect of the vacancy on the displacement of the neighboring Li ions. Taking into account the fact that two close sites are not simultaneously occupied by Li ions, it is convenient to divide the 1-D channel into two types of blocks, as depicted in Fig. S2a: blocks A and A' contain Li3a+, Li3b, and Li3a– sites, whereas blocks B and B' contain Li1a+, Li1b, and Li1a– sites; '+' and '–' distinguish the two split positions above and below the central site, and Li1b is a hypothetical site at an 8*f* position between split Li1(Li1a) sites. We assume that a maximum of one Li ion is located in each of these blocks at one time, with the exception of transient states during migration, which allow double occupancy in one block. Note that there are four 1-D channels in the unit cell, which are labelled as 00, 01, 10, and 11 in Fig. S2a.

The starting model assumed that every block was occupied by one Li ion, which corresponded to $x = 24$ in $Li_x(Ge, P)_6S_{24}$. After the full relaxation of the lattice parameters, internal coordinates, and occupancies for the Li sites, it was found that the Li1b and Li3b sites near the center of the blocks were fully occupied in blocks B(B') and A(A'), respectively, whereas the split Li1a and Li3a sites were completely vacant. This means that the introduction of an Li deficiency is necessary to cause the observed site splitting. Thus, we considered a model with one Li ion missing to give $x = 23$. It was observed that the removal of one Li3b ion from one block A resulted in the lowest energy system, whereas the removal of Li1b, Li2, or Li4 ions gave unstable states that were 0.37 eV, 0.42 eV,

or 0.31 eV higher in energy, respectively. In contrast, the removal of Li2 or Li4 ions caused no splitting in blocks A and B. Moreover, the removal of a Li1b ion from block B resulted in the Li3b ion shifting to Li3a sites in the nearby blocks A and A', but such splitting did not occur for Li1b in the other B blocks. Therefore, the Li deficiency preferably occurred in block A and caused site splitting in both blocks A' and B, as experimentally observed. Schematic views for the distributions of Li ions after relaxation with no deficiency and with one Li missing are shown in Figs. S2b and S3, respectively.

Next, a model with two Li ions removed (x = 22) was considered in order to examine the possible arrangements of two vacancies in the unit cell and investigate the interactions between them. Figure S4 compares five likely models with different arrangements of two vacancies in the A/A' blocks. The relative formation energy was large when the vacancies were in the same channel (0.45 eV), and small when they were in different channels (0 or 0.09 eV). The lowest energy state was obtained when they were located in the A' and A blocks of the 00 and 11 channels, respectively; this arrangement gave a minimum total energy arising from Coulomb repulsions between the vacancies. The other models were not as stable owing to the selection of the neighboring channels 00–01 or 00–10 or that of the same block A' in the 00–11 channels. The occupancies of the Li sites were deduced from the lowest-energy model: g(Li1a) = 0.5, g(Li1b) = 0, g(Li3a) = 0.25, and g(Li3b) = 0.5, and were in good agreement with the experimental values of g(Li1a) = 0.500(9), g(Li3a) = 0.20(2), and g(Li3b) = 0.40(4) from the ND refinements at 10 K. The small values of g(Li3a) and g(Li3b) were due to the fact that the actual Li content in the crystal was $x \sim 21$, i.e., there were three Li deficiencies in the unit cell. The third vacancy must also be located in another block A/A'.

Correlated migration of Li ions

When the arrangements of Li ions in the models of Fig. S4 are carefully examined, it can be seen that the Li ions were not randomly distributed in each the blocks or +, center, or – sites, but followed rules: the two Li ions in B and B' blocks that were separated by an A block came closer to each other when the A block was vacant, whereas only one of the two came closer when the A block was occupied so as to avoid short distances between Li ions in the 1-D channel. In addition, for a 1-D channel without vacancies, the Li ions were either all located at the + or – sites, or all at the center sites. We also note that the correlation between the positions of Li in the neighboring channels did not seem critical, and thus, it is enough to consider hopping processes within a single channel. These observations suggest that the location of Li ions is strongly correlated within the 1-D channel, and, therefore, that Li migration is not governed by a classical single jump process as deduced by the OPP analysis, but rather by a correlated mechanism involving multiple ions.

The migration process of Li ions was considered for transport upward along a 1-D channel with one deficiency each in blocks A and A' of the 11 and 00 channels, respectively, as depicted in Fig. 3a. This corresponds to the lowest-energy model shown in Fig. S4. The process occurs in two steps via transient states, as shown in Fig. 3b. In the first step, the Li ion in block B' moves to the above vacant A block, which is followed by the movement of the Li ion in block A' to block B' (the Li1a site). The former increases the energy as the more stable Li1 site is evacuated, whereas the latter partially compensates for the energy loss. This movement also causes the Li ion in block B to shift

upward from the Li1a– site to the Li1a+ site. In the second step, the Li ion in block B jumps into the vacant A' block, whereas the Li ion in the bottom block A moves to block B (Li1a–), which also pushes the Li ion in block B' from the Li1a– site to the Li1a+ site. As the result, the initial state is recovered via another transient state, and one Li ion is transferred upward to the next unit cell. Note that in each step, two Li ions move cooperatively between nearby blocks, whereas another ion shifts within its original block. Thus, as the all ions do not have to move simultaneously, the migration barrier does not diverge. The potential profile of this correlated migration process was calculated by NEB, and showed a double peak with heights of 0.33 eV, which correspond to the two steps mentioned above, as well as a local minimum of 0.13 eV, as shown in Fig. 3b. Therefore, the effective migration barrier was 0.33 eV, which is much larger than that of the single-ion jump as predicted by the OPP calculation and is in good agreement with the experimental value of 0.29 eV[18].

We also considered the 2-D pathways between Li4 and Li2 sites, which use the Li3–Li1 and Li3 sites in the intervening channels, respectively. A previous study on the former considered a path via Li1 only[40]. However, our NEB calculations showed the stability of vacancies at the Li3 site, and indicated that correlated migration must occur. The corresponding potential profiles are shown in Fig. S5. The effective migration barriers deduced were relatively large; 0.41 eV and 0.59 eV for Li4 and Li2, respectively. These migration barriers were close to those obtained from the OPP calculations and the experimental values, suggesting that the single-ion hopping mechanism works in the 2-D pathways.

References

[1] Kamaya, N.; Homma, K.; Yamakawa, Y.; Hirayama, M.; Kanno, R.; Yonemura, M.; Kamiyama, T.; Kato, Y.; Hama, S.; Kawamoto, K.; Mitsui, A. A lithium superionic conductor. *Nat. Mater.* **2011**, *10*, 682-686.

[2] Whittingham, M. S.; Huggins, R. A. Measurement of sodium ion transport in beta alumina using reversible solid electrodes. *J. Chem. Phys.* **1971**, *54*, 414-416.

[3] Tubandt, C.; Lorenz, E. Molekularzustand und elektrisches Leitvermögen kristallisierter Salze. *Z. Phys. Chem.* **1914**, *87*, 513-542.

[4] Maier, J. Nanoionics: ion transport and electrochemical storage in confined systems. *Nat. Mater.* **2005**, *4*, 805-815.

[5] Yamamoto, O. Solid state ionics: a Japan perspective. *Sci. Tech. Adv. Mater.* **2017**, *18*, 504-527.

[6] Funke, K. Solid State Ionics: from Michael Faraday to green energy—the European dimension. *Sci. Tech. Adv. Mater.* **2013**, *14*, 043502.

[7] Knauth, P.; Tuller, H. L. Solid-State Ionics: Roots, Status, and Future Prospects. *J. Am. Ceram. Soc*. **2002**, *85*, 1654-1680.

[8] Keen, D. A. Disordering phenomena in superionic conductors. *J. Phys. Condens. Matter*, **2002**, *14*, R819.

[9] Takada, K. Progress and prospective of solid-state lithium batteries. *Acta Mater.* **2013***, 61*, 759-770.

[10] Kato, Y.; Hori, S.; Saito, T.; Suzuki, K.; Hirayama, M.; Mitsui, A.; Yonemura, M.; Iba, H.; Kanno, R. High-power all-solid-state batteries using sulfide superionic conductors. *Nat. Energy* **2016**, *1*, 16030.

[11] Wang, Y.; Richards, W. D.; Ong, S. P.; Miara, L. J.; Kim, J. C.; Mo, Y.; Ceder, G. Design principles for solid-state lithium superionic conductors. *Nat. Mater.* **2015**, *14*, 1026-1031.

[12] He, X.; Zhu, Y.; Mo, Y. Origin of fast ion diffusion in super-ionic conductors. *Nat Commun.* **2017**, *8*,

15893.

[13] West, A. R. Ionic Conductivity and Solid Electrolytes. In *Solid State Chemistry and Its Application*, John Wiley and Sons: Chichester, **1984**; pp 452-496.

[14] Hull, S. Superionics: crystal structures and conduction processes. *Rep. Prog. Phys.* **2004**, *67*, 1233-1314.

[15] Catti, M. First-Principles Modeling of Lithium Ordering in the LLTO ($Li_xLa_{2/3-x/3}TiO_3$) Superionic Conductor. *Chem. Mater*. **2007**, *19*, 3963-3972.

[16] Mo, Y.; Ong, S. P.; Ceder, G. First Principles Study of the $Li_{10}GeP_2S_{12}$ Lithium Super Ionic Conductor Material. *Chem. Mater.* **2011**, *24*, 15-17.

[17] Adams, S.; Prasada Rao, R. Structural requirements for fast lithium ion migration in $Li_{10}GeP_2S_{12}$. *J. Mater. Chem.* **2012**, *22*, 7687-7691.

[18] Iwasaki, R.; Hori, S.; Kanno, R.; Yajima, T.; Hirai, D.; Kato, Y.; Hiroi, Z. Weak Anisotropic Lithium-Ion Conductivity in Single Crystals of $Li_{10}GeP_2S_{12}$. *Chem. Mater.* **2019**, *31*, 3694-3699.

[19] Kamaya, N.; Homma, K.; Yamakawa, Y.; Hirayama, M.; Kanno, R.; Yonemura, M.; Kamiyama, T.; Kato, Y.; Hama, S.; Kawamoto, K.; Mitsui, A. A lithium superionic conductor. *Nat. Mater.* **2011**, *10*, 682-686.

[20] Hori, S.; Kato, M.; Suzuki, K.; Hirayama, M.; Kato, Y.; Kanno, R. Phase Diagram of the Li_4GeS_4–Li_3PS_4 Quasi-Binary System Containing the Superionic Conductor $Li_{10}GeP_2S_{12}$. *J. Am. Ceram. Soc.* **2015**, *98*, 3352-3360.

[21] Kwon, O.; Hirayama, M.; Suzuki, K.; Kato, Y.; Saito, T.; Yonemura, M.; Kamiyama, T.; Kanno, R. Synthesis, structure, and conduction mechanism of the lithium superionic conductor $Li_{10+\delta}Ge_{1+\delta}P_{2-\delta}S_{12}$. *J. Mater. Chem. A* **2015**, *3*, 438-446 (2015).

[22] Weber, D. A.; Senyshyn, A.; Weldert, K. S.; Wenzel, S.; Zhang, W.; Kaiser, R.; Berendts, S.; Janek, J.; Zeier, W. G. Structural Insights and 3D Diffusion Pathways within the Lithium Superionic Conductor $Li_{10}GeP_2S_{12}$. *Chem. Mater.* **2016**, *28*, 5905-5915.

[23] Hori, S.; Taminato, S.; Suzuki, K.; Hirayama, M.; Kato, Y.; Kanno, R. Structure–property relationships in lithium superionic conductors having a $Li_{10}GeP_2S_{12}$-type structure. *Acta Crystallographica Section B*, **2015**, *71(6)*, 727-736.

[24] Ohhara, T.; Kiyanagi, R.; Oikawa, K.; Kaneko, K.; Kawasaki, T.; Tamura, I.; Nakao, A.; Hanashima, T.; Munakata, K.; Moyoshi, T.; Kuroda, T.; Kimura, H.; Sakakura, T.; Lee, C.-H.; Takahashi, M.; Ohshima, K.; Kiyotani, T.; Noda, Y.; Arai, M. SENJU: a new time-of-flight single-crystal neutron diffrafctometer at J-PARC. *J. Appl. Cryst.* **2016**, *49*, 120-127.

[25] Petříček, V.; Dušek, M.; Palatinus, L. Crystallographic Computing System JANA2006: General features. *Zeitschrift für Kristallographie - Crystalline Materials* **2014**, *229*, 345-352.

[26] Dysnomia https://doi.org/10.1017/S088571561300002X; 2000.

[27] D. Wiedemann, *OPP_CALC*; 2015.

[28] Blöchl, P. E. Projector augmented-wave method. *Phys. Rev. B* **1994**, *50*, 17953-17979.

[29] Kresse, G.; Furthmüller, J. Efficient iterative schemes for ab initio total-energy calculations using a plane-wave basis set. *Phys. Rev. B* **1996**, *54*, 11169-11186.

[30] Kresse, G.; Joubert, D. From ultrasoft pseudopotentials to the projector augmented-wave method. *Phys. Rev. B* **1999**, *59*, 1758-1775.

[31] Perdew, J. P.; Ruzsinszky, A.; Csonka, G. I.; Vydrov, O. A.; Scuseria, G. E.; Constantin, L. A.; Zhou, X.; Burke, K. Restoring the density-gradient expansion for exchange in solids and surfaces. *Phys. Rev. Lett.*

2008, *100*, 136406.

[32] Liang, X.; Wang, L.; Jiang, Y.; Wang, J.; Luo, H.; Liu, C.; Feng, J. In-Channel and In-Plane Li Ion Diffusions in the Superionic Conductor $Li_{10}GeP_2S_{12}$ Probed by Solid-State NMR. *Chem. Mater.* **2015**, *27*, 5503-5510.

[33] Kuhn, A.; Köhler, J.; Lotsch, B. V. Single-crystal X-ray structure analysis of the superionic conductor $Li_{10}GeP_2S_{12}$. *Phys. Chem. Chem. Phys.* **2013**, *15*, 11620-11622.

[34] Xu, M.; Ding, J.; Ma, E. One-dimensional stringlike cooperative migration of lithium ions in an ultrafast ionic conductor. *Appl. Phys. Lett.* **2012**, *101*, 031901.

[35] Murch, G. E. The Haven ratio in fast ionic conductors. *Solid State Ionics* **1982**, *7*, 177-198.

[36] Wang, J. C.; Gaffari, M.; Choi, S. I. On the ionic conduction in β-alumina: Potential energy curves and conduction mechanism. *J. Chem. Phys.* **1975**, *63*, 772-778.

[37] Watson, G. W.; Parker, S. C.; Wall, A. Molecular dynamics simulation of fluoride-perovskites. *J. Phys., Condens. Matter.* **1992**, *4*, 2097.

[38] Meier, K.; Laino, T.; Curioni, A. Solid-state electrolytes: revealing the mechanisms of Li-ion conduction in tetragonal and cubic LLZO by first-principles calculations. *J. Phys. Chem. C*, **2014**, *118*, 6668-6679.

[39] Deng, Y.; Eames, C.; Chotard, J. N.; Lalère, F.; Seznec, V.; Emge, S.; Pecher, O.; Grey, C. P.; Masquelier, C.; Islam, M. S. Structural and mechanistic insights into fast lithium-ion conduction in Li_4SiO_4–Li_3PO_4 solid electrolytes. *J. Am. Chem. Soc.* **2015**, *137*, 9136-9145.

[40] Du, F.; Ren, X.; Yang, J.; Liu, J.; Zhang, W. Structures, thermodynamics, and Li+ mobility of $Li_{10}GeP_2S_{12}$: a first-principles analysis. *J. Phys. Chem. C*, **2014**, *118*, 10590-10595.

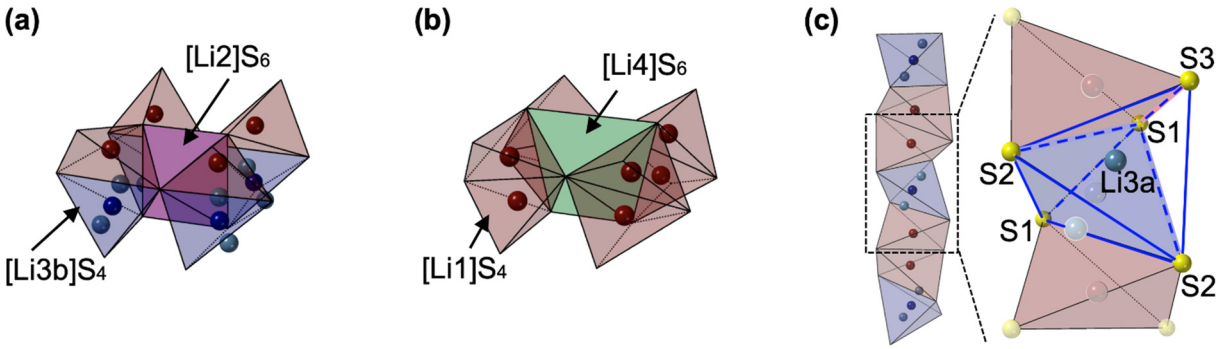

Fig. S1. Coordination environments of Li ions. The $(Li2)S_6$ and $(Li4)S_6$ octahedra are connected with $(Li1)S_4$ and $(Li3b)S_4$ tetrahedra (**a** and **b**), 1-D chain made of face-sharing Li–S tetrahedra along the *c*-axis containing Li1, Li3a, and Li3b sites at 10 K (**c**). The $(Li3b)S_4$ tetrahedron includes two Li3a sites near the shared faces. The Li3a ion can be considered to be coordinated by the five S ions in the trigonal bipyramid shown by the blue lines.

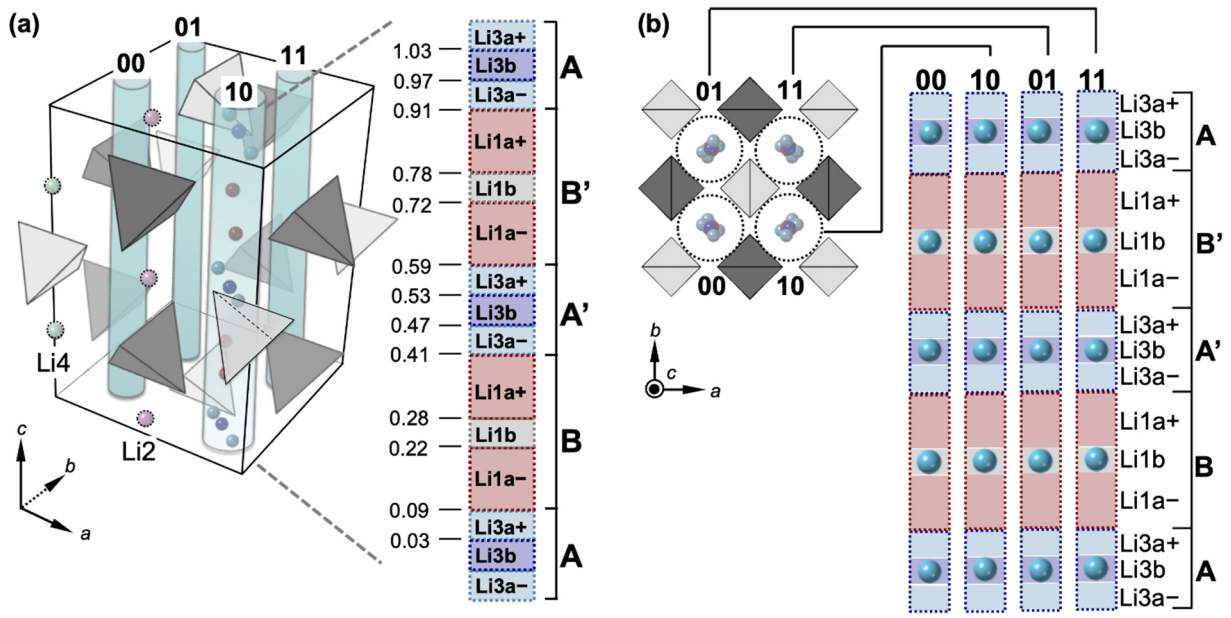

Fig. S2. Schematic representations of the crystal structure of LGPS. **a,** Schematic representations of the crystal structure of LGPS showing all Li sites and the four 1-D channels named 00, 10, 01, and 11 in the unit cell. There are three labeled sites each in a range, defined by the *z*-coordinate. Li1a, Li3a, and Li3b sites are defined to be consistent with the 10 K ND results, whereas Li1b is newly defined as the site between the split Li1 sites. Each 1-D channel is divided into four block types: blocks A and A' contain Li3a+, Li3b, and Li3a– sites, and blocks B and B' contain Li1a+, Li1b, and Li1a– sites. **b,** Stable arrangement of Li positions before removal of Li in $Li_{24}(Ge, P)_4P_2S_{24}$. Light blue balls indicate the position of the Li ion in a given block within channels 00, 10, 01, or 11. Two or more Li cannot simultaneously occupy the same block.

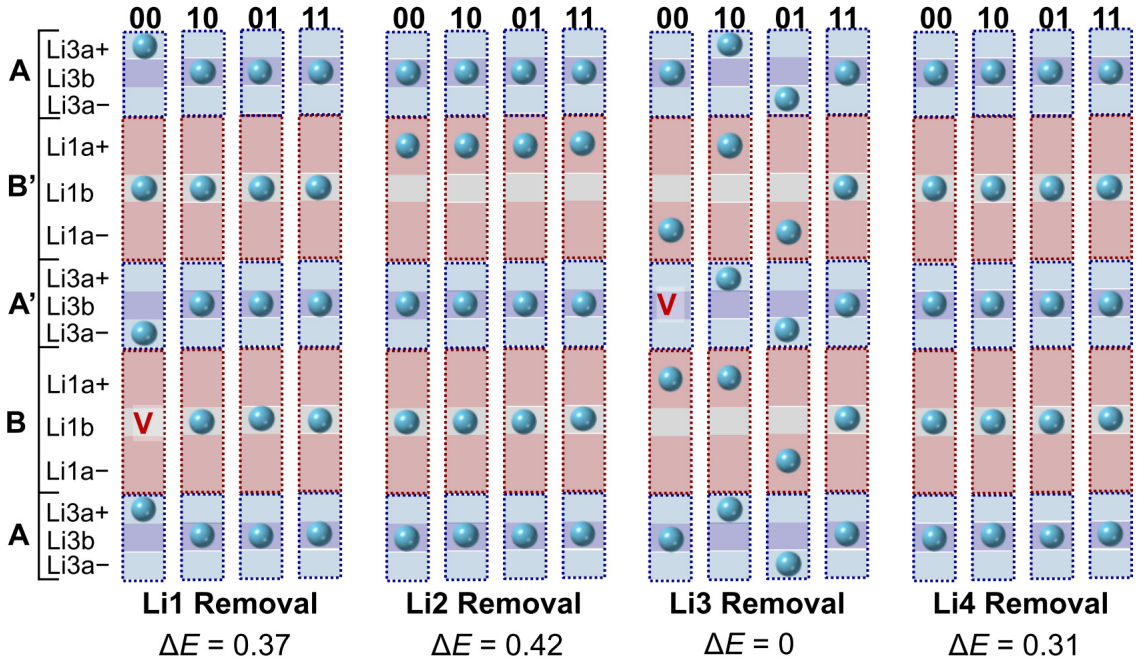

Fig. S3. Representative Li/vacancy configurations and relative energies for $Li_{23}(Ge, P)_4P_2S_{24}$. Light blue spheres indicate the positions of Li ion in channels 00, 10, 01, and 11, whereas 'V' represents a vacant block.

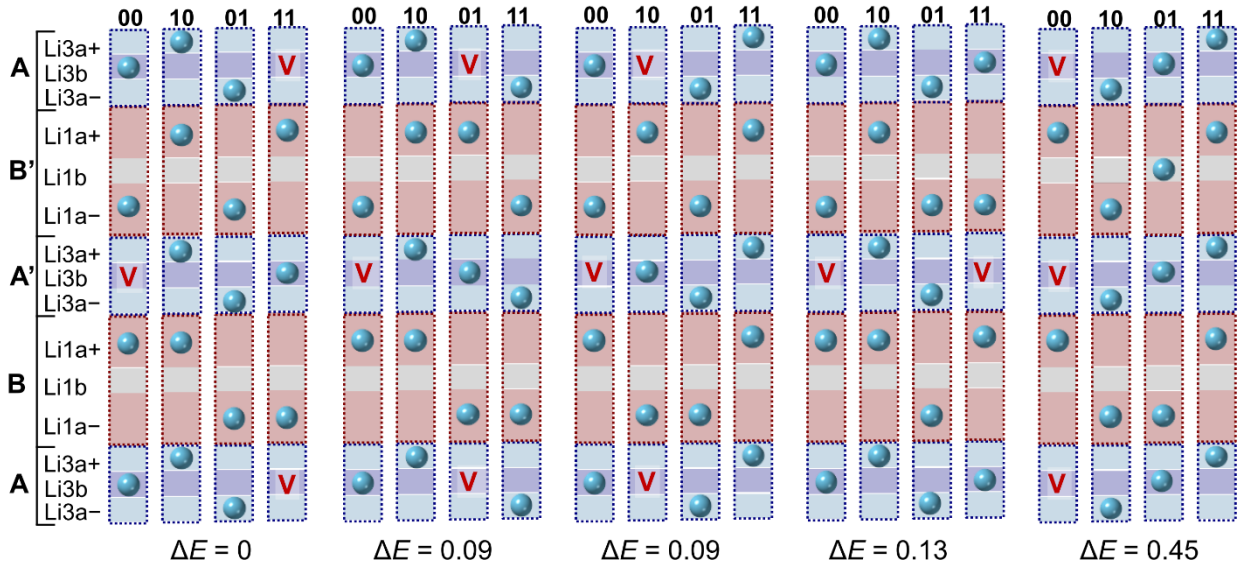

Fig. S4. Representative Li/vacancy configurations and relative energies for $Li_{22}(Ge, P)_4P_2S_{24}$ with two Li ions removed from blocks A/A'.

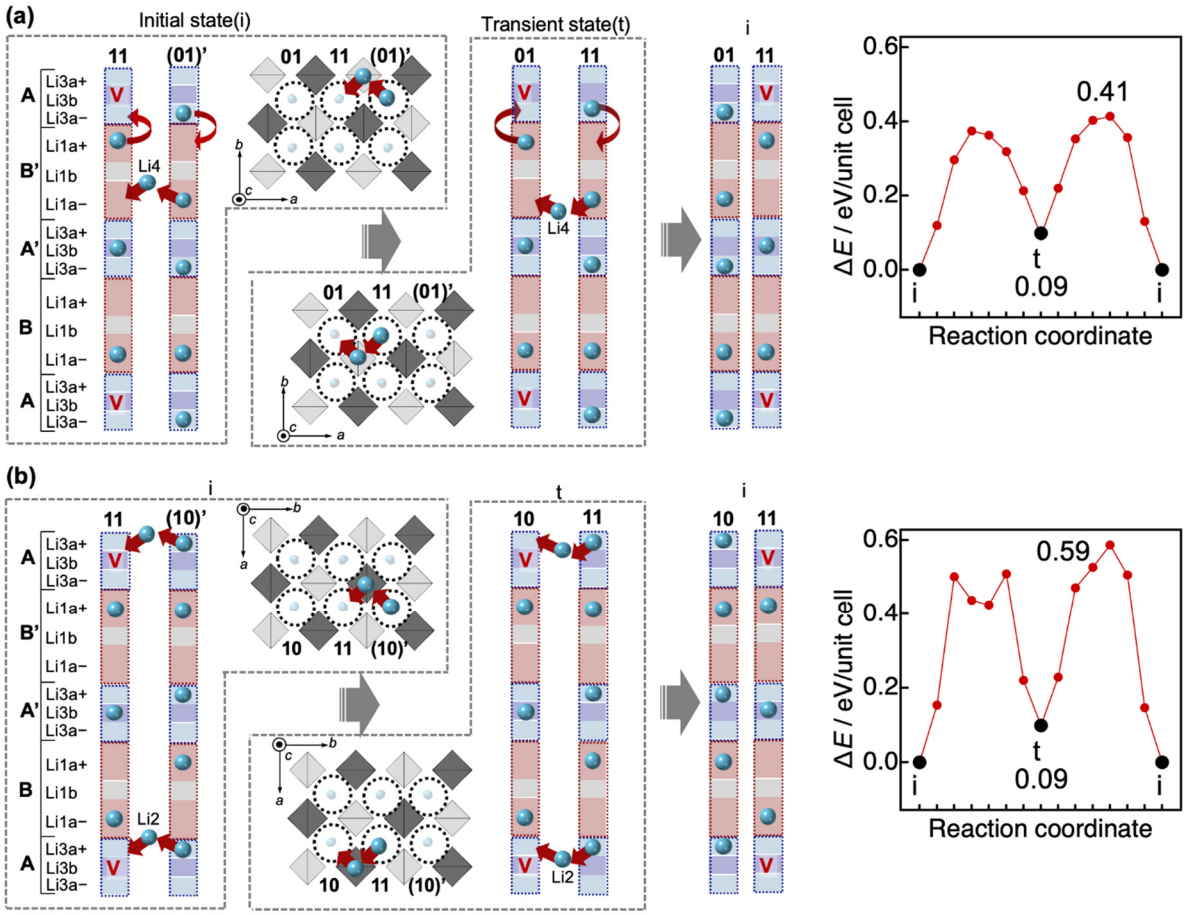

Fig. S5. Correlated migration processes of Li ions and relative energy variations vs reaction coordinate along the 2-D pathways for $x = 22$: **a,** Li1(Li3)–Li4–Li1(Li3) and **b,** Li3–Li2–Li3. In each case, migration occurs via a transient state (t) between the initial, lowest-energy states (i) shown in Fig. 3a. Channels (01)' and (10)' indicate those in the next unit cell. In **a**, the Li ion at Li4 in channel 11 first jumps into the neighboring Li1a– site, and then the vacated Li4 site is occupied by the Li ion at Li1a– in channel (01)' via a jump between channels. These movements trigger rearrangements of the surrounding Li ions both in channels 11 and (01)': the already-present Li ion at Li1a+ in block B' of channel 11 is pushed into the above block A, whereas that in block A of channel (01)' jumps into block B' in the same channel. The resulting transient state is 0.09 eV higher in energy, with an energy barrier of 0.41 eV compared with the initial state. Thus, migration via Li4 sites is accompanied by rearrangements of the Li1 and Li3 sites in the channels. In the Li3–Li2–Li3 path shown in **b**, the Li ion at Li2 of channel 11 jumps into the vacant block A, and then the vacated Li2 site is filled by the neighboring Li ion from block A of channel (10)' via jumping. The transient state is 0.09 eV higher in energy than the initial state, and the energy barrier for this process is 0.59 eV. Although migrations along 2-D pathways are correlated in a similar manner to those in the 1-D channels, the estimated barrier heights are not so different from those for single-ion jumps, suggesting less correlation for migration along the 2-D pathways.

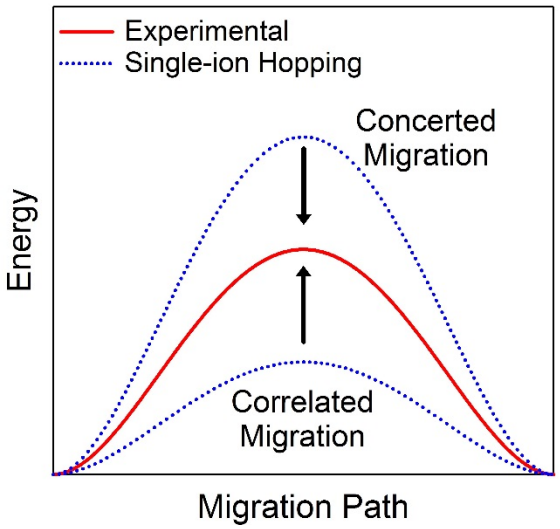

Fig. S6. Schematic representation of the energy landscape for the previous concerted and present correlated migration mechanisms. The former mechanism was proposed to explain the experimental activation energy smaller than the calculated potential barrier for single-ion hopping. However, since the calculated potential barrier was found to be much smaller based on our precise structural data, we propose an alternative mechanism that enhances the effective activation energy that is the correlated migration mechanism.

Table S1. Atomic coordinates and displacement parameters (/Å^2) obtained for the final refinements.

Atom	*Site*	*g*	*x*	*y*	*z*	U_{eq}	U_{11}	U_{22}	U_{33}	U_{12}	U_{13}	U_{23}
(a) XRD data at RT; $Li_{10.34}Ge_{1.34}P_{1.66}S_{12}$, tetragonal $P4_2/nmc$ (137), a = 8.748(14) Å, c = 12.70(2) Å, R_1 = 2.26%, wR_2 = 2.90%												
Li1	16*h*	0.483(15)	0.2603(19)	0.2653(15)	0.1915(15)	0.119(9)	0.086(10)	0.046 (8)	0.23(3)	0.010(7)	0.009(14)	0.006(11)
Li2	4*d*	0.88(4)	0	½	0.9471(8)	0.054(4)	0.057(7)	0.081(8)	0.026(6)	0	0	0
Li3a	16*h*	0.389(13)	0.227(3)	0.256(2)	−0.0346(17)	0.104(13)	0.12(2)	0.045(9)	0.15(3)	−0.023(10)	0.081(19)	−0.039(14)
Li4	4*c*	0.81(9)	0	0	0.2501(11)	0.094(8)	0.052(8)	0.172(18)	0.059(11)	0	0	0
P1	4*d*	0.330(4)	0	½	0.69089(4)	0.02294(17)	0.0277(3)	0.0232(3)	0.0179(3)	0	0	0
Ge1	4*d*	= 1−*g*(P1)	= *x*(P1)	= *y*(P1)	= *z*(P1)	= U_{eq}(P1)	= U_{11} (P1)	= U_{22}(P1)	= U_{33}(P1)	= U_{12}(P1)	= U_{13} (P1)	= U_{23}(P1)
P2	2*a*	1	0	0	½	0.0193(3)	0.0192(4)	0.0192(4)	0.0196(7)	0	0	0
S1	8*g*	1	0	0.18881(8)	0.40700(6)	0.0377(3)	0.0542(5)	0.0231(4)	0.0359(5)	0	0	0.0045(3)
S2	8*g*	1	0	0.29335(9)	0.09599(6)	0.0320(2)	0.0315(4)	0.0366(4)	0.0280(4)	0	0	−0.0041(3)
S3	8*g*	1	0	0.70093(8)	0.79193(6)	0.0296(2)	0.0334(4)	0.0265(4)	0.0288(4)	0	0	−0.0005(3)
(b) ND data at RT; $Li_{10.36}Ge_{1.34}P_{1.66}S_{12}$, tetragonal $P4_2/nmc$ (137), a = 8.704(14) Å, c = 12.61(2) Å, R_1 = 8.17%, wR_2 = 6.58%												
Li1	16*h*	0.515(10)	0.2556(7)	0.2659(5)	0.1860(6)	0.142(5)	0.096(6)	0.023 (4)	0.306(12)	0.030(3)	−0.021(7)	−0.019(5)
Li2	4*d*	0.918(12)	0	½	0.9459(3)	0.0529(19)	0.077(4)	0.059(3)	0.023(2)	0	0	0
Li3a	16*h*	0.361(6)	0.2274(9)	0.2593(8)	−0.0358(5)	0.077(4)	0.096(7)	0.027(4)	0.109(9)	−0.013(4)	0.061(6)	−0.035(5)
Li4	4*c*	0.759(15)	0	0	0.2511(4)	0.082(4)	0.041(5)	0.165(9)	0.041(3)	0	0	0
P1	4*d*	0.33	0	½	0.69079(7)	0.0201(3)	0.0236(6)	0.0198(6)	0.0168(4)	0	0	0
Ge1	4*d*	= 1−*g*(P1)	= *x*(P1)	= *y*(P1)	= *z*(P1)	= U_{eq}(P1)	= U_{11}(P1)	= U_{22}(P1)	= U_{33}(P1)	= U_{12}(P1)	= U_{13}(P1)	= U_{23}(P1)
P2	2*a*	1	0	0	½	0.0171(4)	0.0160(6)	0.0160(6)	0.0192(9)	0	0	0
S1	8*g*	1	0	0.18483(18)	0.40891(13)	0.0274(6)	0.0389(12)	0.0146(9)	0.0286(9)	0	0	0.0016(7)
S2	8*g*	1	0	0.2944(2)	0.09635(12)	0.0277(6)	0.0285(11)	0.0307(11)	0.0238(9)	0	0	−0.0055(8)
S3	8*g*	1	0	0.70029(19)	0.79162(13)	0.0253(6)	0.0283(10)	0.0196(10)	0.0281(9)	0	0	0.0002(8)

(c) ND data at 10 K; $Li_{10.49}Ge_{1.34}P_{1.66}S_{12}$, tetragonal $P4_2/nmc$ (137), a = 8.676(14) Å, c = 12.68(2) Å, R_1 = 8.38%, wR_2 = 6.15%

Li1	16*h*	0.500(9)	0.2527(5)	0.2645(4)	0.1842(4)	0.085(3)	0.067(5)	0.014(3)	0.173(5)	0.022(2)	−0.031(4)	−0.024(3)
Li2	4*d*	0.857(10)	0	½	0.9453(2)	0.0276(14)	0.038(3)	0.036(3)	0.0093(14)	0	0	0
Li3a	16*h*	0.20(2)	0.199(3)	0.2682(11)	−0.0602(14)	0.035(4)	0.047(8)	0.031(6)	0.026(7)	0.015(4)	−0.003(6)	−0.007(4)
Li3b	8*f*	0.40(4)	0.2487(5)	0.2487(5)	0	0.041(8)	0.014(4)	0.014(4)	0.09(2)	−0.009(3)	0.018(7)	−0.018(7)
Li4	4*c*	0.781(12)	0	0	0.2518(3)	0.053(2)	0.021(3)	0.115(6)	0.024(2)	0	0	0
P1	4*d*	0.33	0	½	0.68906(6)	0.0112(3)	0.0145(5)	0.0110(5)	0.0082(3)	0	0	0
Ge1	4*d*	= 1−*g*(P1)	= *x*(P1)	= *y*(P1)	= *z*(P1)	= U_{eq}(P1)	= U_{11}(P1)	= U_{22}(P1)	= U_{33}(P1)	= U_{12}(P1)	= U_{13}(P1)	= U_{23}(P1)
P2	2*a*	1	0	0	½	0.0092(3)	0.0083(5)	0.0083(5)	0.0111(7)	0	0	0
S1	8*g*	1	0	0.18634(16)	0.40828(11)	0.0154(5)	0.0221(9)	0.0076(8)	0.0164(6)	0	0	-0.0020(6)
S2	8*g*	1	0	0.29288(17)	0.09488(10)	0.0150(5)	0.0159(9)	0.0187(9)	0.0102(6)	0	0	-0.0031(7)
S3	8*g*	1	0	0.70140(17)	0.79071(11)	0.0150(4)	0.0199(9)	0.0123(8)	0.0128(6)	0	0	0.0026(6)

Table S2. Selected intersite distances (/Å) at 10 K.

Site1	*Site2*	*Distance*	*Site1*	*Site2*	*Distance*
Li1	Li1	1.688(9) ×1	Li4	Li1	3.287(8) × 4
	Li2	3.545(8) × 1		Li1	3.072(8) × 4
	Li3b	2.339(9) × 1		S1	2.559(7) × 2
	Li4	3.287(8) × 1		S2	3.227(8) × 2
	Li4	3.072(8) × 1		S3	2.646(8) × 2
	Li3a	3.13(2) × 1			
	Li3a	1.68(2) × 1	Li3a	Li1	3.13(2) × 1
	Li3a	3.26(2) × 1		Li1	1.68(2) × 1
	S1	2.482(8) × 1		Li1	3.26(2) × 1
	S2	2.479(8) × 1		Li2	2.650(19) × 1
	S3	2.489(7) × 1		Li3b	0.89(2) × 1
	S3	2.351(8) × 1		Li3a	1.75(3) × 1
				Li3a	3.45(4) × 1
Li2	Li1	3.545(8) × 4		S1	2.279(15) × 1
	Li3b	3.145(8) × 4		S1	3.27(3) × 1
	Li3a	2.650(19) × 4		S2	2.62(2) × 1
	S1	2.761(9) × 2		S2	2.505(14) × 1
	S2	2.613(6) × 2		S3	2.57(2) × 1
	S3	2.625(7) × 2			
Li3b	Li1	2.339(9) × 2			
	Li2	3.145(8) × 2			
	Li3a	0.89(2) × 2			
	S1	2.534(8) × 2			
	S3	2.500(8) × 2			